UNIVERSITI PUTRA MALAYSIA

SYNTHESIS AND OPTICAL CHARACTERISATION OF PbS/Fe3O4 QUANTUM DOTS BY MICROWAVE METHOD AT DIFFERENT TEMPERATURE

MUHAMMAD FADIL BIN MOHD RAZALI

SYNTHESIS AND OPTICAL CHARACTERISATION OF PbS/Fe_3O_4 QUANTUM DOTS BY MICROWAVE METHOD AT DIFFERENT TEMPERATURE

By

MUHAMMAD FADIL BIN MOHD RAZALI

Thesis Submitted to the Department of Physics, Universiti Putra Malaysia, in partial Fulfilment of the Requirements for the Degree of Bachelor of Science (Hons.) in Physics

January 2022

DEDICATION

This dissertation is dedicated to my parents, Muhd Razali bin Abdul Ghani and Saripah bt Mamat who have provided me with continuous love, support, and inspiration.

ABSTRACT

Synthesis and Optical Characterisation of PbS/Fe_3O_4 Quantum Dots by Microwave Method at Different Temperature

by

Muhammad Fadil Bin Mohd Razali

197106

January 2022

Supervisor : Dr. Mazliana Ahmad Kamarudin

Faculty : Faculty of Science

In this work,we report the synthesis of PbS/Fe_3O_4 core shell QDs by using microwave methods at different temperatures. The PbS acts as the core was synthesized using a colloidal method with DTG and TGL as capping ligands. The Fe_3O_4 nanoparticles act as the shell is synthesised using chemical co-preparation technique. The formation of Fe_3O_4 was confirmed by the X-ray diffraction (XRD) . The result shows that Fe_3O_4 nanoparticles were magnetite and the size is approximately 19 nm in powder form. The PbS/Fe_3O_4 core shell QDs were characterized by UV-Vis and PL spectroscopy. We observed that the PL peak were redshifted as the synthesized temperature of PbS/Fe_3O_4 increases from 45,55, and 55 °C. This could be due to the increase of Fe_3O_4 shell thickness that give an effect on the carrier confiment. Next, the full width half maximum (FWHM) decreased when growing shell on PbS core at 50 ^oC and then increased at temperature 55 ^oC. From UV-Vis, the result shows that the sample is semiconductor as the bandgap

energy is from 0-3 eV. Lastly, band gap energy from PL and UV-Vis is not same because of Stokes shift. As conclusion, we succesfully synthesised and characterised magnetite Fe_3O_4 powder and PbS/ Fe_3O_4 CSQDs

ABSTRAK

Sintesis dan Karakterisasi PbS/Fe_3O_4 Teras/Petala Titik Kuantum dengan Kaedah Ketuhar Gelombang Mikro Pada Suhu Berbeza

Oleh

Muhammad Fadil Bin Mohd Razali

197106

Januari 2022

Penyelia : Dr. Mazliana Ahmad Kamarudin

Fakulti: Fakulti Sains

Dalam kajian ini, kami melaporkan sintesis PbS/Fe_3O_4 teras petala titik kuantum (CSQDs) menggunakan kaedah ketuhar kelombang mikro pada suhu yang berbeza. PbS bertindak sebagai teras disintesis menggunakan kaedah koloidal dengan DTG dan TGL sebagai ligan penutup. Nanozarah Fe_3O_4 bertindak sebagai petala disintesis menggunakan kaedah pemendakan kimia. Pembentukan Fe_3O_4 telah disahkan oleh analisis belauan sinar X (XRD). Hasil kajian menunjukkan Fe_3O_4 adalah magnetit dan bersaiz kira-kira 19 nm dalam bentuk serbuk. Teras petala titik kuantum PbS/Fe_3O_4 dianalisis dengan menggunakan UV-Vis dan spektroskopi fotoluminesens (PL). Kami memerhatikan bahawa graf PL menunjukkan ajakan merah apabila suhu PbS/Fe_3O_4 meningkat daripada 45,55, dan 55 °C. Ini mungkin disebabkan oleh peningkatan ketebalan petala Fe_3O_4 yang memberi kesan kepada pengurungan pembawa. Seterusnya, lebar separuh ketinggian maksimum (FWHM) berkurangan apabila tumbuh petala pada teras PbS pada 50 ℃ dan kemudian meningkat pada suhu 55 ℃. Daripada UV-Vis , keputusan menunjukkan bahawa sampel adalah semikonduktor kerana tenaga jurang jalur adalah dari 0-3 eV. Akhir sekali,

tenaga jurang jalur daripada PL dan UV-Vis tidak sama kerana anjakan stoke. Sebagai kesimpulan, kami berjaya mensintesis dan menganalisis serbuk Fe_3O_4 magnetit dan PbS/ Fe_3O_4 CSQDs

ACKNOWLEDGEMENT

First and foremost, praises and thanks to God, the Almighty, for His showers of blessings throughout my research work to complete the research successfully. I would like to express my deepest gratitude to my supervisor, Dr. Mazliana Ahmad Kamarudin for her continuous support, motivation, and guidance towards me through the theoretical and practical knowledge in this research. It is a great experience to work under her guidance.

I am very grateful for having three awesome seniors who are also involved in the nanoSEM area, namely Safwan, Kak Dian and Kak Afifah. I would like to thank them for giving advice and brilliant ideas about my project. Other than that, I would like to give a special thanks to my fellow friends, Ambok and Adlin for being kind to share their ideas and help me greatly when I am in need.

Next, many thanks to the lab assistant who helped with the characterization. It is hard for me to do my research without them. Finally, I'd like to express my gratitude to my family. Thank you for your love, encouragement, and support.

TABLE OF CONTENT

CHAPTER 4 RESULTS AND DISCUSSIONS

CHAPTER 5 CONCLUSIONS

LIST OF FIGURES

.

LIST OF TABLES

LIST OF ABBREVIATIONS

CSQDs	Core-shell quantum dots
QDs	Quantum dots
PbS	Lead Sulphide
PbS/Fe_3O_4	Lead sulphide/iron oxides
QY	Quantum yield
LEDs	light-emitting diodes
TSQDs	Thick-shell QDs
PL	Photoluminescence
FWHM	Full width at half maximum
NIR	Near-infrared
CQDs	Colloidal quantum dots
TGL	Thioglycerol
DTG	Dithioglycerol
MAPbI	Methylammonium lead iodide ligands
PC	Propylene carbonate
DFP	Difluoropyridine
PbSe	Lead selenide
QLEDs	Quantum dot light-emitting diodes
MRI	Magnetic resonance imaging

M-S	Microwave-sonochemical
XRD	X-ray Diffraction
UV-Vis	Ultaviolet-Visible
HOMO	Highest occupied molecular orbital
LUMO	Lowest unoccupied molecular orbital
HBM	Hyberpobic band model
FWHM	Full width half maximum

CHAPTER 1
INTRODUCTION

The first chapter will introduce the quantum dots, type of core-shell quantum dots (CSQDs), bandgap engineering and application of quantum dots. Followed by the problem statements and objectives of the research.

1.1 Quantum Dots

The developments of colloidal semiconductor nanocrystal or quantum dots (QDs) have become a phenomenon because of extraordinary optical and electronic characteristics (Moreels et al., 2009). A Russian physicist, Alexei Ekimov, first discovered quantum dots in the 1980s (Kargozar et al., 2020). Colloidal QDs are typically manufactured using wet-chemical synthetic processes that are both affordable and scalable (Kagan et al., 2016). QDs are semiconductor materials that composed of approximately 10^2 to 10^4 atoms with sizes from 2 to 10 nm in which we can tune their optoelectronic properties (Alizadeh-Ghodsi et al., 2019). QDs are semiconductor crystals that are nanoscale in size and have a physical dimension smaller than the exciton Bohr radius, resulting in exceptional electronic properties due to the quantum confinement effect (Zaini et al., 2019). At ambient temperature, Lead Sulphide (PbS) has band gap of 0.4 eV and a relatively large exciton Bohr radius of 18 – 20 nm (Touati et al., 2015). If we synthesis PbS QDs smaller than 18–20 nm, we can term it PbS QDS. In Pbs QDs, the movement of the exciton is confined in zero dimension due to the size of quantum dots are comparable or smaller than exciton Bohr radius, thus the band

gap energy increases with QDs size decrease. This phenomenon is known as quantum confinement or quantum size effect (Zaini et al., 2020).

1.2 Types of core-shell Quantum dots

Quantum dots are coated in organic surfactants to achieve and maintain quantum confinement, but the organic surfactant lowers luminous quantum yield (QY). this problem can be overcome by growing an epitaxial layer of inorganic material over quantum dots core which formed core-shell QDs (CSQDs). As a result of this, CSQDs improve photoluminescence efficiency due to the increased dangling bonds on the surface of QDs and confinement of electrons and hole pair in the core (Vasudevan et al., 2015). We can determine the types of CSQDs in the nanocrystal semiconductor based on the size of band gaps and position of the valence band and conduction band in CSQDs(Reiss et al., 2009). There are four main types of CSQDs which are type I, inverse type I, type II and inverse type II. The band gap of the core is narrower than the band gap of the shell in type I, therefore excited electrons and holes are entirely confined in the core. The PbS/MnS (Zaini et al., 2019) CSQDs is one example of type I CSQDs. For inverse type I such as CdS/CdSe (Jin et al., 2017), the band gap of the core is higher than band gap of shell thus the excited electrons and holes are completely or partially confined in shell. Next, in a type II system, one charge carrier is mostly confined to the core, whereas the other is mainly confined to the shell, with the core's valence band edge within the shell's band gap. The example of type CSQDs is CdTe/CdSe. In inverse Type II CSQDs like lnP/CdS, the conduction band edge of the core lies within the band gap of the shell, and one excited electron is delocalized in the core/shell structure while the other is trapped within the core (AbouElhamd et al., 2019). In this study, we

synthesize lead sulphide/iron oxides (PbS/Fe_3O_4) CSQDs that are classified as inverse type I as shown in figure 1.2.1 since the band gap of the Pbs core is 0.4 eV (Touati et al., 2015) and the band gap of the Fe_3O_4 shell is 0.1 eV (Marand et al., 2014).

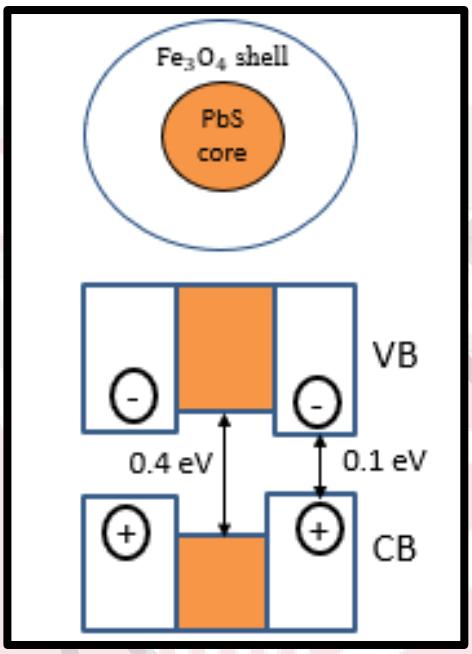

Figure 1.2.1 : Inverse type I PbS/Fe_3O_4 CSQDs

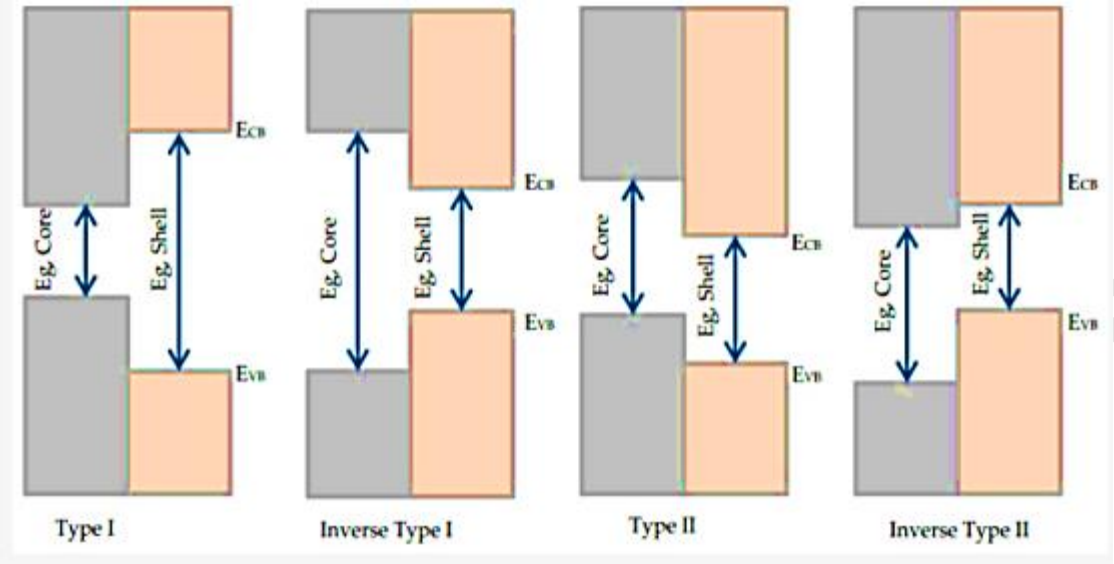

Figure 1.2.2: Types of core-shell semiconductors (AbouElhamd et al., 2019).

1.3 Bandgap Engineering

The size, shape, and composition, band-Offset tuning of core and shell, impurity doping, strain tuning of core and shell are the parameters in the nanocrystal that can tune their electronic band gaps. Because of quantum confinement, the band gaps of most semiconductors can be shifted by more than 1 eV, allowing for an enormous range of continuous tunability through size and shape for a single material composition (Smith & Nie, 2010). The number of overlapping orbitals or energy levels reduces as the particle size of semiconductor nanomaterials approaches the nanoscale, and the conduction and valence band thickness decrease. The energy band gap between the valence and conduction bands will increase due to particle reduces to nanoscale (Singh et al., 2018). Impurity doping is one of the ways to tune the band gap by providing an intraband electronic level that allows lower energy light emission from the defect state to the ground state, as seen in

figure 1.3. The energy band gap can also be tuned by modifying the chemical composition of QDs. For example, the energy band gap of ZnSe is greater than that of CdSe. The transition from type I (carrier is localized within core) to type II CSQDs causes electron and hole segregation between the core and shell materials in core-shell semiconductor heterostructures or the carrier localized in the core and shell. Furthermore, the band gap size of the core and shell of that material may be altered by increasing shell thickness or strain tuning. For instance, when the ZnSe shell thickens, the size of the shell's band gap decrease (figure 1.3), resulting the electrons localized to the shell and holes localized to the core where carrier recombination can occur at lower energy and higher wavelength between this interface (Smith & Nie, 2010).

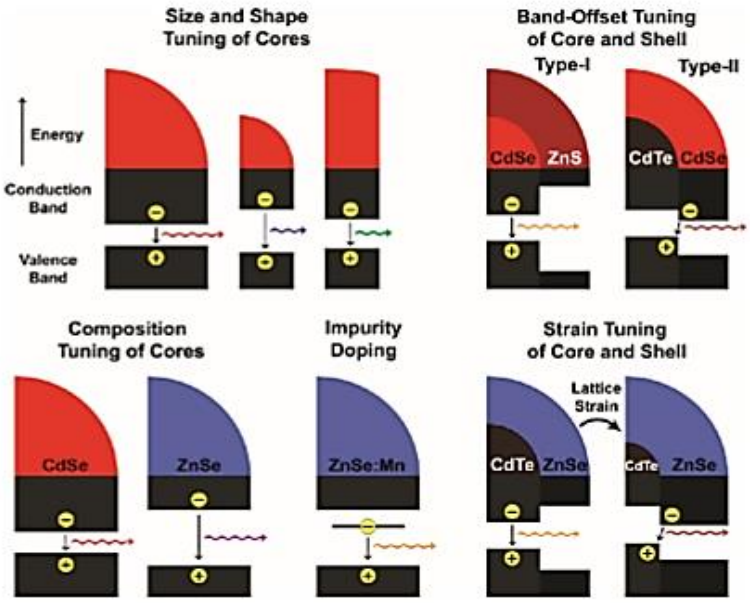

Figure 1.3: Mechanisms of bandgap engineering in semiconductor nanocrystals through size, shape, composition, impurity doping, heterostructure band offset, and lattice strain (Smith & Nie, 2010)

1.4 Application of Quantum dots

Organic fluorescent dyes and genetically encoded fluorescent proteins have shown to be useful tools for bioimaging applications throughout the last decades, but with the advancement of nanotechnologies, QDs are being incorporated into bioimaging and diagnostics (Bilan et al., 2016). QDs have significant advantages over traditional fluorescent organic dyes and green fluorescent proteins. This is due to photobleaching, low signal intensity, and spectral overlap in organic dyes compare to multiple fluorescence colors, high signal brightness, long-term photostability, and multiplex capabilities in QDs (Liu et al., 2011).

Next, colloidal quantum dots are suited for use as the emitting layer in light-emitting diodes (LEDs) due to their customizable colors, strong emission, solution processability, and stability (Frecker et al., 2016). Thick-shell QDs (TSQDs) were typically produced by epitaxial growth of inorganic shells on the cores to remove surface defects states. Thus, improving chemical stability and photoluminescence (PL) quantum yield (QY) with no change in their tunable emission and narrow full width at half maximum (FWHM). As a consequence, QDs with pure color emission with FWHM smaller than 30 nm may be generated in different colour range (Hao et al., 2019).

1.5 Problem statement

The larger-sized PbS QDs have a quantum yield (QY) of between 20% and 40% with an emission peak in the 1300-1600 nm region. This is because the emission of bigger QDs may be easily quenched by localized trap states, whereas smaller QDs emitting in the 1100-1300 nm range have a quantum yield of 60 to 90 percent. To present, developing a viable strategy for producing PbS-based QDs with high QY in the telecommunication wavelength region (1300-1550 nm) has been difficult (Ren et al., 2013). Recent studies revealed that core/shell approach is one of the most efficient way to produce high QY near-infrared (NIR) emitting QDs (Ren et al., 2013). In this study, we created inverse type – I PbS/Fe_3O_4 CSQDs having PbS as the core an Fe_3O_4 as the shell and analyzed the sample using photoluminescence (PL) spectroscopy. Therefore, we predict that PbS/Fe_3O_4 inverse type I CSQDs will exhibit higher PL intensity or QY with a larger energy band gap.

However, producing CSQDS using conventional heating in oil bath produced non uniform growth of shell and introduced defects in thicker shell (Ren et al., 2013). We adopted the microwave-assisted technique to overcome this problem where the previous studies showed that microwave assisted synthesis produced CdSe/ZnS core/shell QDs with a very rapid reaction time, limited size distribution, and outstanding optical characteristics (Ren et al., 2013). Other benefits of the microwave-assisted approach include quick volumetric heating, fast reaction rates, spontaneous nucleation events, repeatability, and size and shape control via reaction parameter control (Purcar et al., 2021).

1.6 The objective of the research

The objectives of this research are:

I. to synthesis colloidal PbS QDs as control sample and PbS/ Fe_3O_4 CSQDs with different shell thicknesses by varying temperature reactions in the microwave-assisted method.

II. to examine the optical properties of PbS QDs and PbS/Fe_3O_4 CSQDs with different shell thicknesses by using photoluminescence (PL) spectroscopy.

.

CHAPTER 2
LITERATURE REVIEW

This chapter will present the ligands capped with PbS QDs, near infrared (NIR) emitting QDs, Quantum Yield (QY), Fe_3O_4 shell, The inverse type I Core/Shell QDs (CSQDs) and method to Synthesis Core-Shell QDs

2.1 The ligands capped with PbS QDs

Colloidal quantum dots (CQDs) are semiconducting nanocrystals coated with ligands, as seen in Figure 2.1. The Ligands provide electrostatic repulsion to stabilize QDs and avoid from aggregating uncontrollably in the solvent. Previously discussed capping agents or ligands include thiobutanol, thiohexanol, triglycolic acid, thioglycerol (TGL), and dithioglycerol (DTG). TGL and DTG were combined to produce high-quality nanocrystals (Bakueva et al., 2004). That is why we synthesized PbS QDs using the process described by (Zaini et al., 2019), who employed a colloidal approach using TGL and DTG as ligands. The use of atomic ligands in CQDs is a powerful method for tuning their characteristics and improving charge carrier transport in CQD solids (Bederak et al., 2018). Zhao et al revealed that water-soluble PbS nanoparticles stabilized with a thiol mixture (TGL and DTG) indicated efficient, stable infrared photoluminescence centred in the 1050-1200 nm, full width at half-maximum (FWHM) of the PL emission peak was from 70 to 100 nm, photoluminescence quantum efficiency at room temperature was from 7 to 10% (Zhao et al., 2005). Other than that, oleic acid capped with PbS showed that OA-PbS nanoparticles were found to be monodispersed spherically shaped nanoparticles with particle diameters ranging from 2.91

to 10.05 nm for PbS produced at 150 °C. The particle sizes increased to 9.26 – 29.08 nm at 190 °C and 17.96–88.07 nm at 230 °C (Ajibade & Oluwalana, 2020). For PbS CQDs capped with methylammonium lead iodide ligands (MAPbI 3), the efficiency of propylene carbonate (PC) and 2,6-difluoropyridine (DFP) as solvents was examined. The results demonstrated that both solvents have good colloidal stability for 80 days since the initial excitonic peak location and optical density are the same.

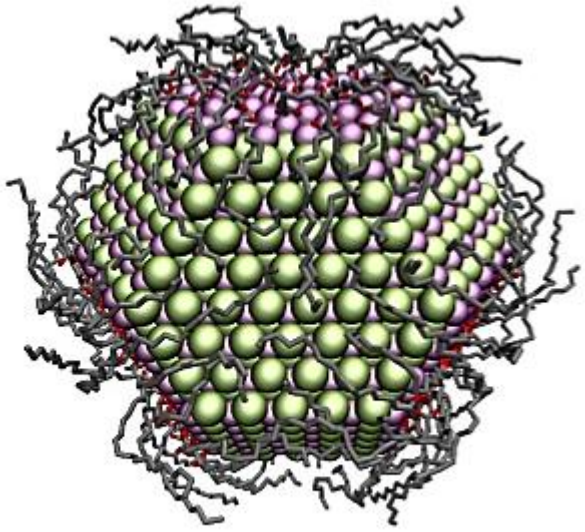

Figure 2.1: Model of lead sulfide quantum dot with ligand coverage (Sohn, 2018)

2.2 Near infrared (NIR) emitting QDs

NIR emitting lead QDs have attracted the attention of researchers because of their potential uses in bioimaging, solar cells and telecommunications. These QDs emission may be tuned in range of 750 to 3700 nm. (Pichaandi & Van Veggel, 2014). There many types of NIR emitting QDs such as PbS nanocrystal (Hines & Scholes, 2003), Lead selenide (PbSe) CQDs (Pichaandi & Van Veggel, 2014), PbSe/PbS CSQDs (Aeberhard et al., 2012), and InAs (ZnCdS) QDs (Allen et al., 2010). QDs can be used for bioimaging because they have high brightness, photobleaching resistant, can be activated by a single wavelength, and can emit wavelengths which are significantly different from bulk. NIR QDs with these distinctive features can be used as contrast agents in optical imaging, particularly in deep tissue imaging.(Aswathy et al., 2010). Then, with minimal photon scattering, in vivo fluorescence imaging in the 1,500-to-1,700 nm region provide more clarity and deeper tissue penetration (Zhang et al., 2018). Therefore, in our study we want to improve emission peak of PbS QDs in PL that emit wavelength in range of 1300-1550 nm.

2.3 Quantum Yield (QY)

The purpose of this research is to improve the fluorescence of Pbs-based QDs. The effectiveness of turning absorbed light into emitted light, which can take the form of fluorescence, was referred to as quantum yield (QY). The QY is an important metric for determining a fluorophore's optical quality (Laverdant et al., 2011). To generate high efficiency quantum dot light-emitting diodes (QLEDs), begin with a high-QY quantum dot emitter, where the excited state is formed by electron-hole recombination (Yang et al., 2017). The photoluminescence QY, also known as the fluorescence QY. Fluorescence QY defined as the ratio of photons emitted to photons absorbed (Resch-Genger & Rurack, 2013). Demas and Crosby examined quantum yield measuring techniques in solution in 1970, and further advances were made possible by instrumental breakthroughs. A fluorophore solution's absorption is typically determined by passing a light source via the solution and determining the input and output powers (Laverdant et al., 2011). As a function of QD size, concentration, excitation photon energy, and storage conditions, the QY of colloidal PbS QDs capped with OA in toluene as a solvent has received a lot of attention. They noticed an abnormal reduction in QY with decreasing concentration in extremely diluted solutions caused by ligand desorption and QD-oxidation. The stability of QD colloidal suspensions increases as the concentration and size of PbS QDs increase. (Greben et al., 2015).

2.4 Fe_3O_4 shell

Fe_3O_4 nanoparticles have fascinating features such as superparamagnetism, enormous surface area, low toxicity, and biocompatibility (Tzafaras et al., 1981). There is various method to synthesi Fe_3O_4 such as co-precipitation (Khalil, 2015; Sagala et al., 2021; Tzafaras et al., 1981) microwave-sonochemical (C. Li et al., 2013),hydrothermal (Ahmadi et al., 2012) and solvothermal (Yan et al., 2008). Previous research on co-precipitation, sonochemical, and solvothermal methods found that nanoparticles created by co-precipitation had the smallest size, while XRD patterns revealed that nanoparticles created by solvothermal methods had the highest crystallinity, Fe_3O_4 particles formed spherical by co-precipitation and solvothermal methods, and TGA curves revealed that the Fe_3O_4 nanoparticles formed by sonochemical approach had the maximum thermal stability (Mahmud et al., 2020). The co-precipitation method developed by (Daoush, 2017) revealed that magnetite powder has a spherical formed with size of 30 nm, a face-centered cubic crystal structure, a super magnetic character, a squarness ratio of 0.14, and the ability to be used as a contrasting agent in magnetic resonance imaging (MRI) diagnosis. The average crystalline, physical size, saturation magnetization, and coercivity of Fe_3O_4 nanocrystal increased with hydrothermal temperature (100,150,200 ^oC) while applying the hydrothermal technique (Ahmadi et al., 2012). Microwave-sonochemical (M-S) methods are superior to conventional solvothermal methods because magnetite has a smaller size, greater magnetism, and is manufactured on a large scale (C. Li et al., 2013).

2.5 The inverse type I Core/Shell QDs (CSQDs)

CSQDs are the product of further engineering in quantum dots. They have better optical qualities than ordinary QDs because of the shell that surrounds the QD core, which increases stability and photoluminescence efficiency (Stride & Mirnajafizadeh, 2020). The formation of a shell on core nanocrystals can improve their QY and photobleaching resistance, as well as minimize fluorescence emission blinking. Due to these features, core/shell nanocrystals are increasingly being used as luminous biological probes and active materials in light emitting diodes (LEDs) (Mahler et al., 2012). PbS/Fe_3O_4 CSQDs are classified as reverse type I systems because a material with a narrower band gap is grown over a material with a wider band gap (Reiss et al., 2009). Besides PbS/Fe_3O_4 CSQDs, CdS/CdSe CSQDs (Pan et al., 2012), CdSe/PbS (Wieliczka et al., 2018) and $Cd_{0.1}Zn_{0.9}$ S/CdSe (Jin et al., 2017) are also reverse type I CSQDs. The shell's conduction and valence bands are localized within the core's band gap in inverse type-I system. As a result, the holes and electrons are confined within the shell (Stride & Mirnajafizadeh, 2020). Figure 2.5 illustrates reverse type-I $Cd_{0.1}Zn_{0.9}$ S /CdSe QDs with a high PL QY (61%) at 625 nm wavelength and extensively tunable emission extending from 450 to 670 nm. An electroluminescence (EL) peak at 631 nm was redshifted to the solution PL spectrum by 6 nm (625 nm) (Jin et al., 2017). As the thickness of the CdSe shell surrounding the CdS cores increases, both the absorption onset and the band-edge PL emission peaks move to the long-wavelength side (red shift) in PL spectra, as seen in figure 2.6 (Pan et al., 2012). For CdSe/PbS, with increasing shell thickness, the absorption and photoluminescence (PL) band edge characteristics shift to lower energies, but still above the CdSe bulk band gap (Wieliczka et al., 2018).

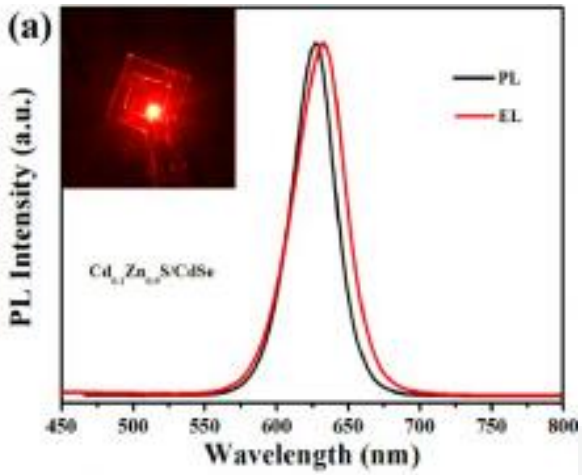

Figure 2.5 : The electroluminescence (EL) and PL spectrum of $Cd_{0.1}Zn_{0.9}$ S /CdSe (Jin et al.,2017)

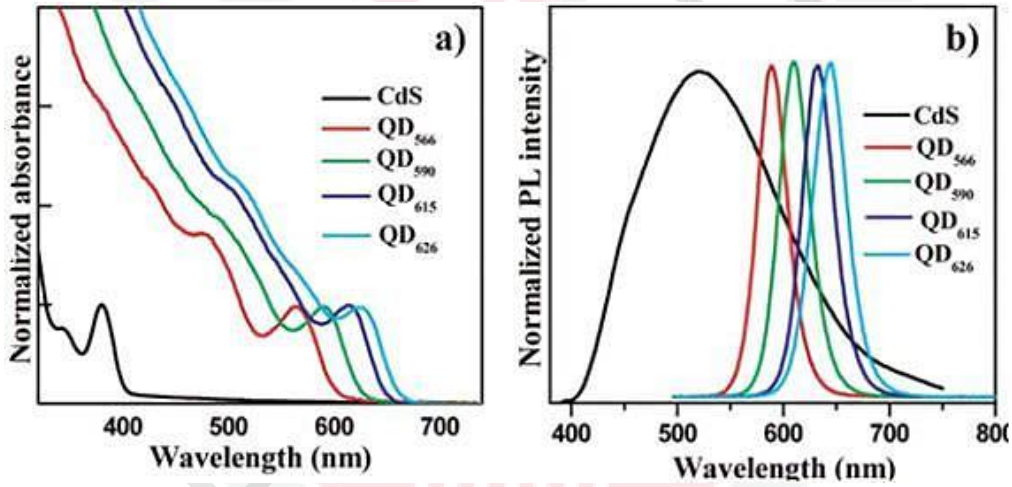

Figure 2.6 : CdS and derivate CdS/CdSe core/shell QD absorption (a) and PL spectra (b) with different absorption onsets (Pan et al., 2012).

2.6 Method to Synthesis Core-Shell QDs

They are various method in producing core/shell nano-heterostructures (NHs) like co-precipitation (Peng et al., 1997), successive ionic layer adsorption and reaction (SILAR) (J. J. Li et al., 2003), microwave radiation (Baghbanzadeh et al., 2011), organometallic (Mekis et al., 2003) and microemulsion (Kortan et al., 1990). A microwave-assisted synthesis is a popular approach for synthesis of nanocrystals because of the benefits of high efficiency and reaction selectivity in getting controlled products. Microwave-assisted CdTe/CdSe type II quantum dots in aqueous solution had good crystallinity, enhanced photoluminescence quantum yield (PLQY) from 12% to up to 45% and the emission wavelength was adjustable from 530 to 680 nm by changing the reaction time to increase in shell thickness (Sai & Kong, 2011). The PbS/CdS type I CSQDs that synthesize via microwave-assisted cation exchange manufactured monodisperse QDs with emission wavelengths ranging from 1300 to 1600 nm, QY as high as 57 % (Ren et al., 2013). Figure 2.5a demonstrated that the reaction temperature was raised by conventional heating in an oil bath, resulting in a variable reaction rate and shell growth that was not uniform, whereas figure 2.5b demonstrated uniform shell growth (Ren et al., 2013).The microwave-assisted approach provides for the quick synthesis of aqueous CdTe/CdS core-shell nanocrystals. This is due to the fact that CdTe/CdS core-shell nanocrystals had a high PLQY (up to 75 percent) with no post-preparative treatment and a narrow particle size distribution (fwhm about 35 nm). Microwave irradiation is ideal for speeding epitaxial development of the CdS shell since it only takes 5 minutes to generate an optimal thickness (1.9 nm) of the CdS shell in the microwave assisted method (He et al., 2006).

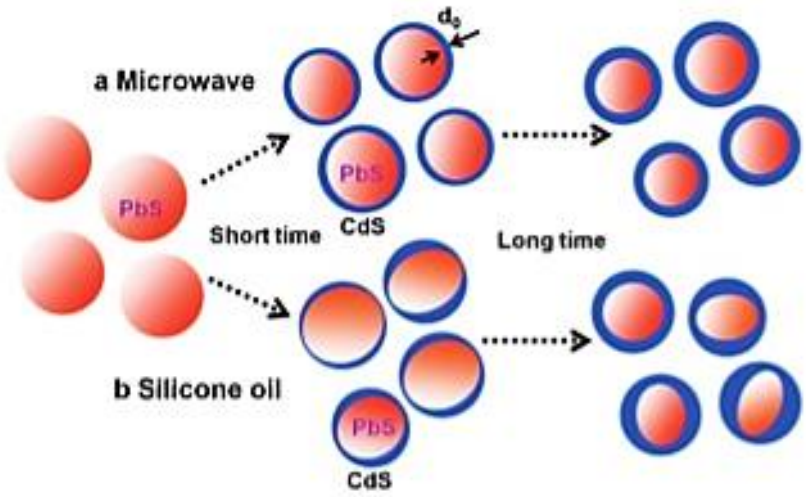

Figure 2.7: The predicted PbS/CdS QDs development pattern during cation exchange: The heating methods used were (a) microwave assisted technique and (b) silicone oil bath heating (Ren et al., 2013)

CHAPTER 3
METHODOLOGY

This chapter will focus on how PbS quantum dots (QDs), Fe_3O_4 shell and PbS/Fe_3O_4 core/shell QDs (CSQDs) were synthesized and the basic principle of X-ray diffraction (XRD),Ultraviolet-visible(UV-Vis) and Photoluminescence (PL) spectroscopy.

3.1 Materials and apparatus

The list of materials used to synthesis PbS/Fe_3O_4 CSQDs is shown in Tables 3.1

Table 3.1: List of material used to prepare PbS/Fe_3O_4 CSQDs

Material	Present state	Chemical formula
Lead (II) Acetate	Solid crystal	$C_4H_6O_4Pb.3H_2O$
Sodium Sulfide	Solid crystal	$Na_2S.9H_2O$
Deionized water	liquid	H_20
1-Thioglycerol (TGL)	liquid	$C_3H_8O_2S$
di – thioglycerol (DTG)	liquid	$C_3H_8OS_2$
Triethylamine	liquid	$C_6H_{15}N$
Nitrogen gas	gas	N_2
Iron chloride	Solid crystal	$FeCl_3$
Distilled water	Liquid	H_2O
Potassium iodide	Solid crystal	KI
Sodium Hydroxide	Solid crystal	NaOH

3.1.1 Preparation of PbS QDs

Firstly, we synthesized Pb^{2+} precursor by preparing 0.1889 g of lead (II) acetate ($C_4H_6O_4Pb.3H_2O$) and 45 ml of deionized water (H_2O). Then, we injected the deionized water into the three-neck flask by passing it through a boat polystyrene containing lead (II) acetate. At the same time, nitrogen gas,N_2 is being flow into the three-conical flask to remove oxygen, and a magnetic stirrer is being used to mix the solution. Then, the Pb^{2+} precursor was allowed to dissolve for 15 minutes at room temperature.

After that, by using a micropipette, 388.5 µL of TGL was added to the three-conical flask, followed by 149.7 µL of DTG. The TGL and DTG capping ligands were added to prevent agglomeration. The addition of capping ligands, changed the solution from colorless to yellowish-green. Then, triethylamine was added to the solution drop-wise to adjust the pH until it reached pH 11. As it reached pH 11, the solution change from yellowish green to colorless. To prepare S^{2-} precursor, 0.0359 g of Na_2S was added into 1.4953 ml of deionized water in a beaker. After a S^{2-} precursor is fully dissolved, we used a 5 ml syringe to transfer it into the Pb^{2+} precursor. The both precursors were fixed with 400 rpm and the solution changes from colorless to dark brown. This dark brown solution indicated the formation of PbS QDs. The production of PbS QDs in aqueous solution was carried out according to the process described by Bakueva et al., with a size of about 4.00 ± 1.00 nm and a molar ratio of Pb^{2+} to S^{2-} of 1: 0.5 (Bakueva et al., 2004)

Later, we transferred the PbS QDs into a vial, which was firmly wrapped with parafilm and aluminium foil, as illustrated in Fig. 3.1.1. Finally, after four hours of synthesis, the sample was placed in a refrigerator, which is a dark and low-temperature environment.

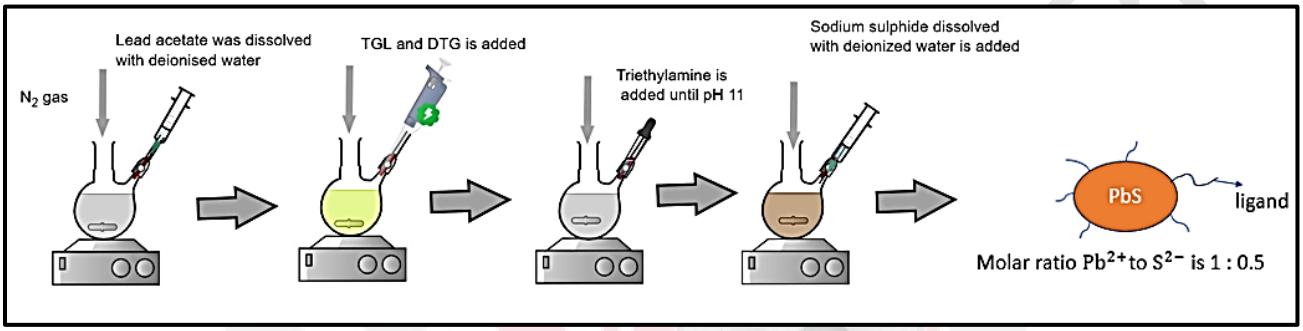

Figure 3.1. The schematic figure of preparation of PbS QDs with capping ligands.

Figure 3.1.1 The PbS QDs in vial wrapped with aluminium foil and parafilm.

3.1.2 Preparation of Fe_3O_4 shell

The Fe_3O_4 shell nanoparticles was synthesized by the co-precipitation method. This technique is the safe to use, affordable, consumes less time, and has a high productivity. It also has the benefit of generating high purity, having an uncomplicated process, and requiring a low synthesis temperature (Sagala et al., 2021). In our co-precipitation method, we prepare solution A and solution B. For solution A, we dissolved 4.866 g of iron chloride ($Fecl_3$) in 37.82 ml distilled water while for solution B, we dissolved 1.660 g of potassium iodide (KI) in 12.63 distilled water. The solution A (0.7933 M) and B (0.7920 m) were mixed, stirred and allow to reach equilibrium for one hour at room temperature.

The filter paper was used to filter away the iodine precipitate after an hour. The filtrate was then hydrolyzed with a 76 mL NaOH solution, which was added dropwise with constant stirring until pH 11 was attained and black magnetite precipitate emerged. After that, the setup was given an hour to settle. The precipitation will be divided into two layers, with a transparent phase at the top and a black precipitate phase at the bottom. A clear phase was extracted using a syringe, and the precipitate was washed with distilled water and ethanol.

After washing, the precipitate was sun-dried to produce Fe_3O_4 powder. After that, the powder was ground and sieved. To obtain 0.1 M of Fe_3O_4 in liquid formed , we weighted 0.185 g of Fe_3O_4 and added 8 ml distilled water .This was followed by 30 minutes of sonication with a sonicator. After filtering with membrane filter , the precipitate's color turned to a light yellowish color that showed Fe_3O_4 nanoparticles is obtained.

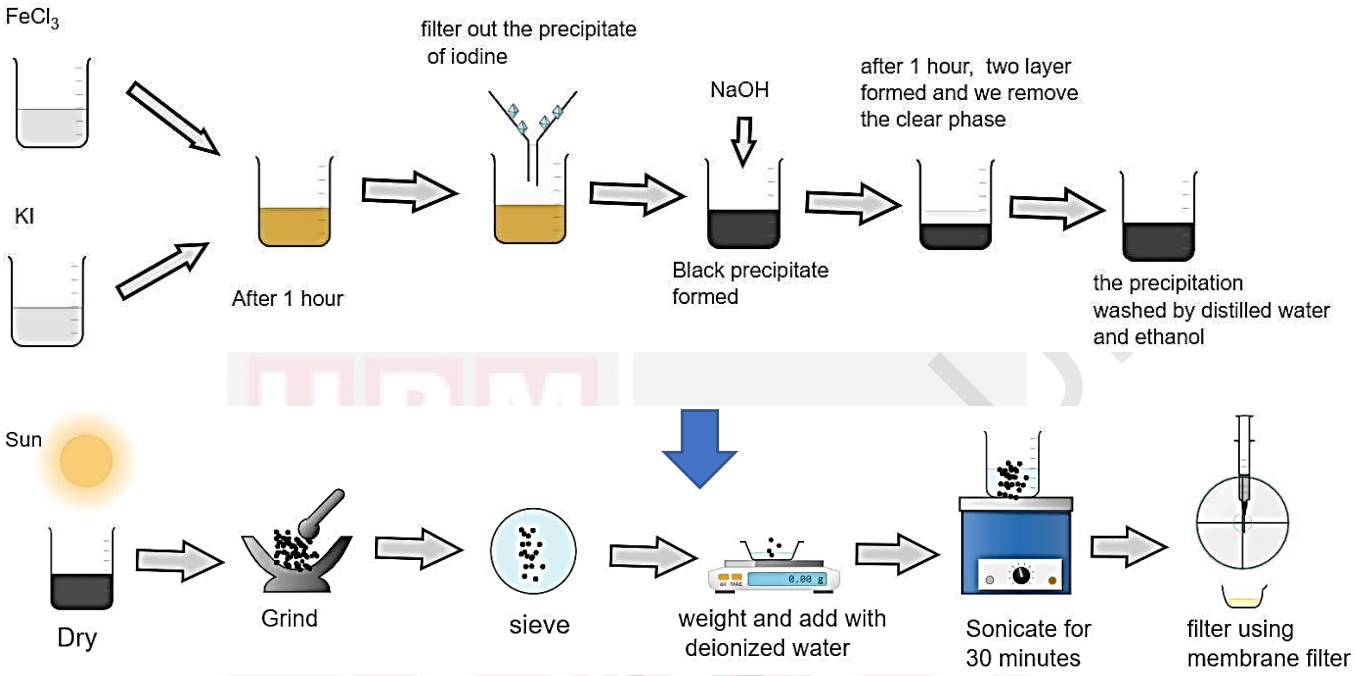

Figure 3.1.2: The schematic figure for preparation of Fe_3O_4

3.1.3 Preparation of PbS/Fe_3O_4 CSQDs

Microwave-assisted synthesis was used to produce the PbS/Fe_3O_4 CSQDs. In this study, we employed Monowave 400/200 microwave reactors, which are capable of producing small-scale microwave synthesis applications. Then 0.1 ml Fe_3O_4 nanoparticle and 5 ml PbS QDs was added into a test tube of microwave. The mixture was irradiated for 1 minutes at temperature 45,50 and 55 ^oC. Each sample of PbS /Fe_3O_4 CSQDs were then transfer into degassed vial and kept under 4 ^oC at dark.

3.2 X-Ray Diffraction (XRD)

X-rays with wavelengths ranging from 10^{-3} to 10^{1} nm are produced within an evacuated X-ray tube by bombarding a metal target (anode) with high-velocity electrons. Monochromatic X-rays used for X-ray diffraction(XRD) have finite energy and wavelength characteristics for the specific target metal (Lagally, 1985). When a collimated beam of monochromatic X-rays of wavelength meets a crystal, the rays penetrate and are partially dispersed from many successive planes within the crystal, as seen in figure 3. There will be a critical angle, for a given interplanar spacing, d, at which rays dispersed from successive planes will be in phase as they exit the crystal. A ray going down the path BPB' from figure 3.2, will have travelled nλ wavelengths farther than a ray travelling along the path ADA'. The angle formed by the normal to the emerging wave front and the atomic planes will be the same as the angle formed by the normal to the primary wave front and the atomic planes. Diffraction from a series of similarly spaced lattice planes produces a diffraction maximum with enough intensity to be recorded. When the Bragg law, $n\lambda = 2d \sin$, is satisfied, diffraction can occur (Lagally, 1985). The XRD is a popular technique for characterising nanoscale materials. XRD analysis of a sample gives valuable information which are phase identification, sample purity, crystallite size, and morphology. From the graph of intensity against 2θ, As the size of the crystallite decreases from bulk to nanoscale dimensions, the width of the peak expand . There are one equation that can determine the size of nanoparticle which is Scherrer equation ,$D=\frac{k\lambda}{\beta\cos\theta}$. The symbol D refer to crystalline domain size, k is Scherrer constant that usually assumed to be 0.9, The wavelength of X-rays (λ) is a constant that depends on the type of

X-rays generated, width of the peak at half of its height (β) and (θ) is peak at a spesific diffraction angle (Holder & Schaak, 2019).

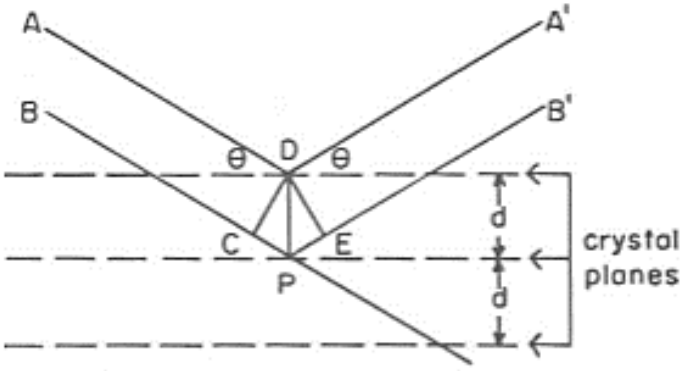

Figure 3.2 : Diffraction from crystal planes according to Bragg's law, $n\lambda = 2d \sin\theta$ (Lagally,1985)

3.3 Ultraviolet-visible (UV-Vis) absorption spectroscopy

UV-Vis absorption is based on the concept that matter's energy content is quantized and that photons of radiation can be absorbed or emitted by matter if the energy associated with the photon equals the energy difference for permissible transitions of that particular species. The transitions represented are those that may be produced by UV light absorption. The process by which energy from a photon of electromagnetic radiation is transmitted to the absorbing substance is known as radiation absorption. When an atom or molecule absorbs a photon of light, its internal energy increases by the amount of energy stored in that photon. As a result, during the absorption process, the electron transitions from a lower energy state to a more excited state. (Penner, 2017). Lambert-Beer's law is applied in UV-Vis and the equation as presented in equation 3.3,

$$A = -\log T = \log \frac{I_o}{I} = \varepsilon.c.d \qquad (3.3)$$

Where A is absorbance, T is transmission, I_o is intensity of the measuring beam before passing through the sample, I is intensity of measuring beam after passing through the sample, ε is molar absorption, c is concentration and d is path length of the measuring beam in the sample (Mäntele & Deniz, 2017).

3.4 Principle of Photoluminescence (PL) spectroscopy

Photoluminescence (PL) spectroscopy is a great technique for researching semiconductors and electronic devices since it is non-destructive and non-invasive (Abdi-Jalebi et al., 2019). PL is a process in which electron is exciting from ground state to excited state and the electron recombine to ground state with emission of photons. In solid state physic, PL can be divided into fluorescence and phosphorescence and one of the difference between them is phosphorescence lifetime is longer (1 ms to 10 ms) than fluorescence lifetime which is in the range of 0.1-10 ns (Matsuoka et al., 2012).

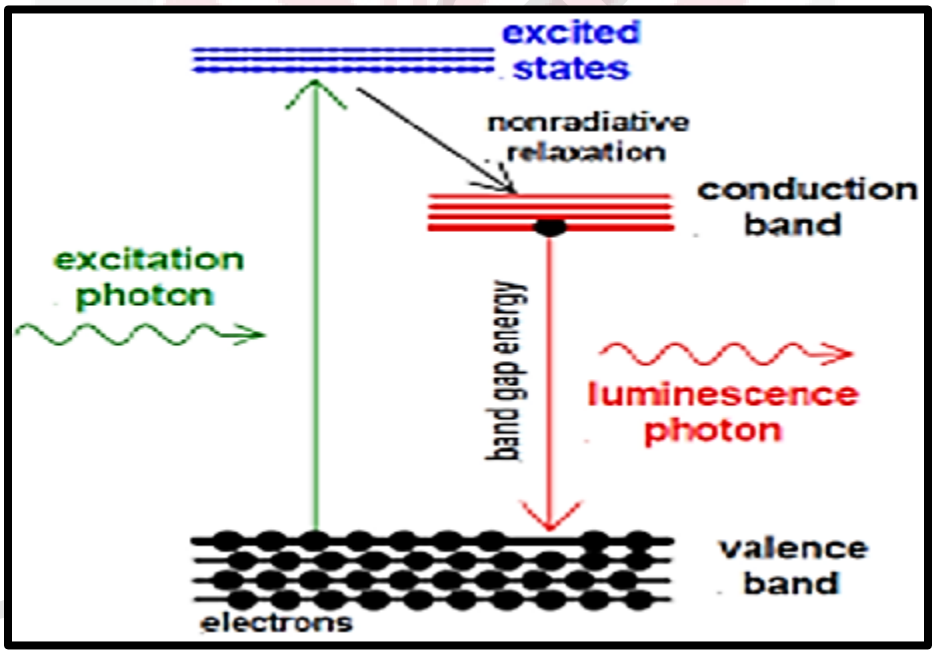

Figure 3.4: Principle of Photoluminescence Spectroscopy (Vallikkodi, 2018)

The electrons at valence band or highest occupied molecular orbital (HOMO) absorb energy higher than band gap energy from laser (excitation photon) to jump at conduction band or lowest unoccupied molecular orbital (LUMO). Then, electron will return to their equilibrium states that include the emission of light whether a radiative process (luminescence photon) or non-radiative process as shown in figure 3.2. Typically, the radiative transition is from conduction band to valence band with energy difference is known as band gap. From PL spectroscopy, we can identify optical band gap, purity, impurity defect levels of semiconductor material (Vallikkodi, 2018).

CHAPTER 4

RESULTS AND DISCUSSION

This chapter presents the characteristics of PbS quantum dots (QDs) and PbS/Fe_3O_4 core shell QDs. The samples were characterized via XRD,UV-Vis and photoluminescence. The result of each measurement will be discussed.

4.1 X-ray diffraction (XRD) of Fe_3O_4

Figure 4.1 shows the XRD pattern of Fe_3O_4 particles. From the analysis, it was found that the crystal structure of magnetite Fe_3O_4 is cubic with a lattice parameter of a=b=c= 8.3750 x 10^{-10} m . The value is match with the standard data (JCPDS Card No 01-088-0315). The Miller indices that were obtained from Figure 4.1 were (220), (311), (400), (422), (511), (440) for the Fe_3O_4 powder at 2theta of 30.16°, 35.53°, 43.18°, 53.57°, 57.11°, and 62.71°, respectively. The result were well matched with work done by Habtemariam et. al. (Habtemariam, 2021; Khoshnam & Salimijazi, 2021) The crystalline size of Fe_3O_4 can be determined from the XRD pattern using the Debye-Scherrer formula, $D = k\lambda / \beta \cos\theta$ (where k = 0.9, λ = 0.154 nm, β = the reflection width (311) crystal plane, θ = the Bragg angle). The findings indicate that the magnetic core's crytallite size is approximately 19.10 nm (Khoshnam & Salimijazi, 2021).

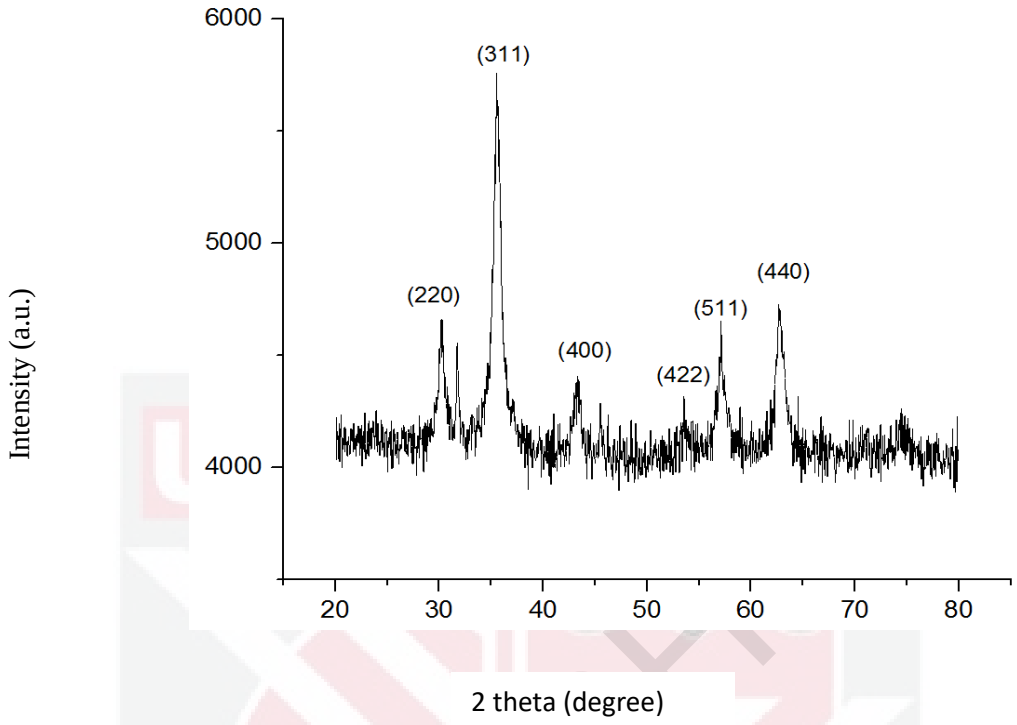

Figure 4.1 : The X-ray diffraction pattern of the Fe_3O_4 particles

4.2 UV–Vis absorption of PbS quantum dots (QDs) and PbS/Fe_3O_4 core shell QDs

PbS quantum dots (QDs) and PbS/Fe_3O_4 core shell QDs have a brown dark colour. The Uv-Vis device cannot be used with dark samples because they absorb light. Therefore , we diluted each sample with buffer, which changes the colour of the sample to light yellow. Then.the analysis is carried out with the touc plot on origin software. As a result, we were able to determine the band gap of each sample as show in table 2. By using touc plot, we found that the direct bandgap energy is 2.23 eV while indirect bandgap energy is 1.06 eV for PbS QDs. For PbS/Fe_3O_4 CSQDs, the direct bandgap energy are 2.27 eV,2.19 eV and 2.21 eV while indirect bandgap energy are 1.00 eV,1.37 eV,1.25 eV as temperature increase from 45,50,55 ^oC respectively. As the value of bandgap energy is from 0 to 3 eV, we can consider our material is semiconductor (Strehlow & Cook, 1973).

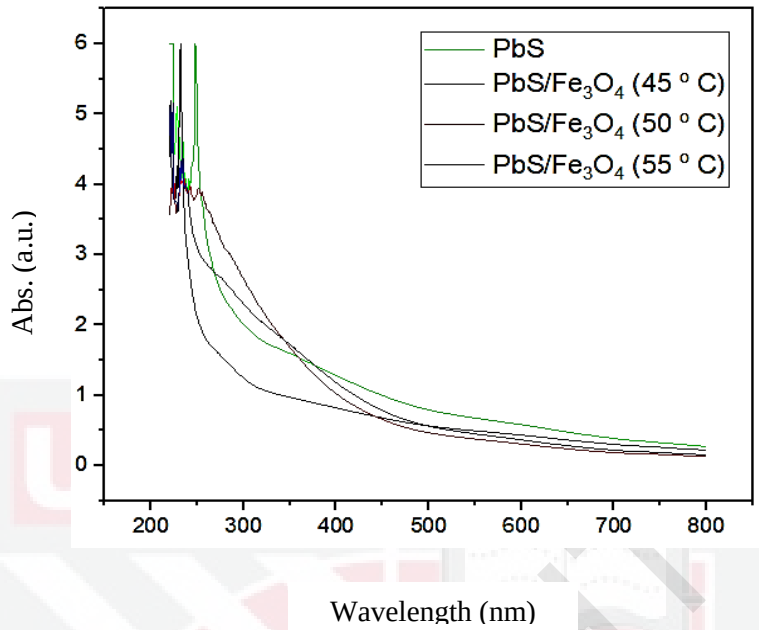

Figure 4.2 : The UV-vis absorption of PbS and PbS/Fe_3O_4 at different temperature

Table 4.2 : Band gap of PbS and PbS/Fe_3O_4 at different temperature

Sample	Indirect Bandgap energy (eV)	Direct Bandgap energy (eV)
PbS QDs	1.06	2.23
PbS/Fe_3O_4 core shell QDs (45 ℃)	1.00	2.27
PbS/Fe_3O_4 core shell QDs (50 ℃)	1.37	2.19
PbS/Fe_3O_4 core shell QDs (55 ℃)	1.25	2.21

4.3 Photoluminescence of PbS quantum dots (QDs) and PbS/Fe_3O_4 core shell QDs

Figure 3 shows the PL emission of sample PbS and PbS/Fe_3O_4 was run at room temperature. PL from PbS QDs was emitted at the wavelength of 1610 nm which is longer than reported by Bakueva et. al. (1250 nm). This difference is due to the intervals during the measurement thus cause the change of QDs size due to Ostwald ripening. For samples PbS/Fe_3O_4 prepared at temperature of 45, 50 and 55 ℃, the PL was emitted at 475,506 and 539 nm, respectively. The different on PL peak emission between PbS and PbS/Fe3O4 is noticeable as listed in Table 4.3. These peaks are similar with PL peak emission reported by Sadat et. al.We believe that the carrier recombination occur in the region of Fe_3O_4 in sample PbS/Fe_3O_4 QDS. The schematic figure in Figure 4.4 shows charge carrier are partially delocalised within the shell in inverse type 1 system (Vasudevan et al., 2015). As the synthesize temperature of PbS/Fe_3O_4 increase, the wavelength emission was increased ; band gap energy decreased. This is due to the shell thickness of Fe_3O_4 is getting thicker (Zhong et al., 2005).

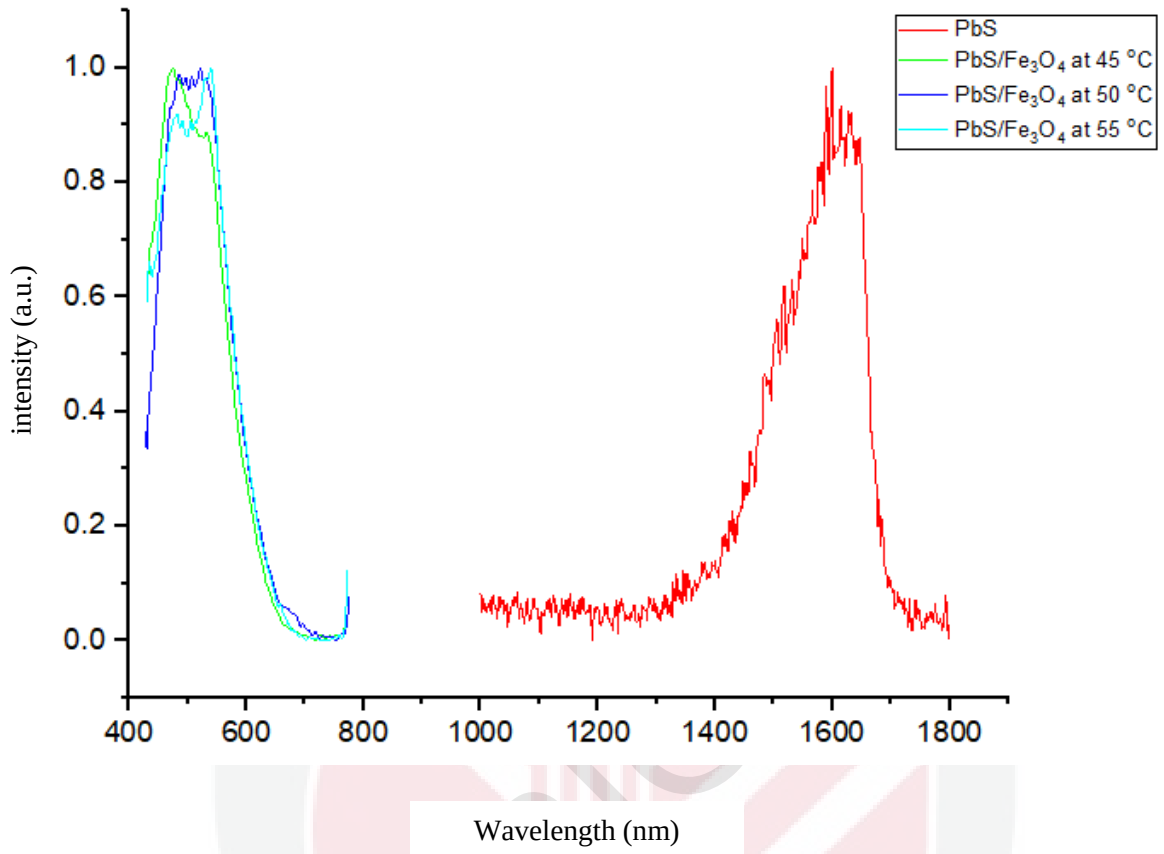

Figure 4.3 : Normalized Photoluminescence of PbS and PbS/Fe_3O_4 at different temperature

Table 4.3 : Band gap energy and wavelength emission PbS quantum dots (QDs) and PbS/Fe_3O_4 core shell QDs

Sample	**Bandgap energy from PL(eV)**	**Wavelength emission (nm)**
PbS QDs	0.77	1610
PbS/Fe_3O_4 core shell QDs (45 ℃)	2.61	475
PbS/Fe_3O_4 core shell QDs (50 ℃)	2.45	506
PbS/Fe_3O_4 core shell QDs (55 ℃)	2.30	539

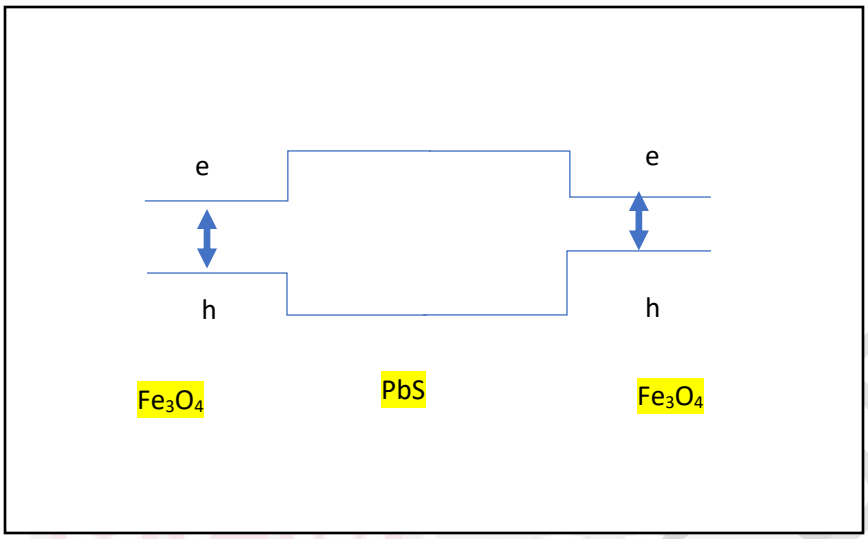

Figure 4.4 : Charge carrier partially delocalised within the Fe_3O_4 shell

4.4 The effect of quantum confinement of PbS and PbS/Fe_3O_4

The estimation of QDs size can be calculate use Brus equation. The reason we applied Bruss equation because it was the best approximation to the experimental result with TEM images compared to hyperbolic band model (HBM), the Henglein model and Yu equation (Rodríguez-Mas et al., 2020). The Brus equation as presented in Equation (4.4),

$$E_{g(QD)} = E_{g(bulk)} + (h^2\pi^2/2R^2) \times (1/m_{e^*} + 1/m_{h^*}) - (1.8e^2/4\pi\varepsilon_o\varepsilon_r R) \qquad (4.4)$$

Where $E_{g(QD)}$ is bandgap energy of quantum dots, $E_{g(bulk)}$ is bandgap energy of bulk semiconductor (PbS=0.41 eV), h is Plank's constant, R is Radius of quantum dots, m_{e^*} is effective mass values of electrons (PbS= 0.085 x mass of electron), m_{h^*} is effective mass values of holes (PbS=0.085 x mass of electron), e is fundamental charge of electron, is ε_o dielectric constant in vacuum and ε_r is dielectric constant of medium.

The radius of the PbS core is 4.96 nm based on PL emission $E_{g(QD)}$ = 0.77 eV, (Nanda et al., 2004). As the diameter is about 10 nm , the PbS core QDs experienced strong quantum confinement because size of PbS is less than 18 nm of exciton bohr radius (Zaini et al., 2020). Next, when we coated PbS QDs with Fe_3O_4 shell , PL energy is decreased from 2.61 eV,2.45 eV , to 2.30 eV with increased temperature from 45,50,55 ℃ . Because the band gap energy is inversely proportional to wavelength, as PL energy decreases, the emission spectra become red shifted due to the formation of a shell around the core (Subramanian et al., 2020). On other hand, the UV-vis result show a different value of band gap energy from PL because of Stokes shift (AbouElhamd et al., 2019).

4.5 The effect of shell thickness on the size distribution of CSQDs

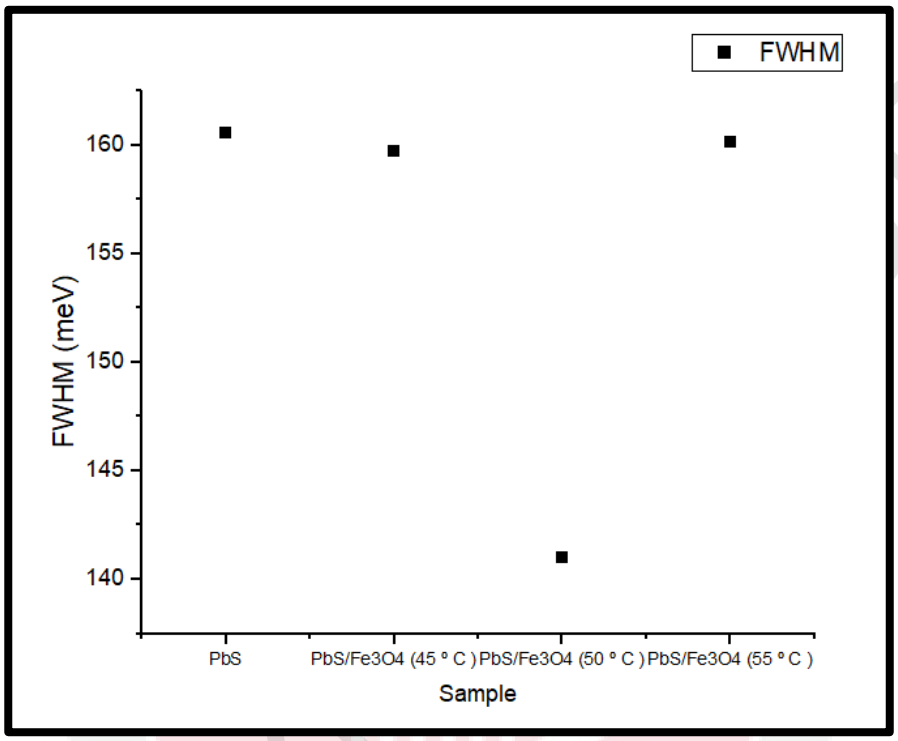

Figure 4.5 : FWHM of PbS and PbS/Fe_3O_4 CSQDs with different temperature from 45 to 55 ^oC

Figure 4.5 shows the graft of full width half maximum(FWHM) of PbS QDs and PbS/Fe_3O_4 CSQDs with different microwave temperature from 45 ^oC to 55 ^oC . We can observe that the FWHM was decreased from 160.5502 to 141.0267 meV when growing Fe_3O_4 shell onto PbS core at 55 ^oC . This is because the PL curve becomes symmetric as the shelling process occurs (Jin et al., 2017). However, the further growth of the Fe_3O_4 shell leads to increasing of FWHM from 141.0267 to 160.12 meV. This is probably because Fe_3O_4 does not homogenously coat the PbS core (Vale et al., 2016). We conclude that the temperature in the microwave affected the shell

thickness of Fe_3O_4. Increasing the temperature of the microwave will lead to a growing Fe_3O_4 shell thickness. Since the Fe_3O_4 shell becomes thicker, the bandgap energy or emission energy becomes lower and shifted to red. Also, FWHM exhibits a narrow size distribution and it tends to be uniform and homogenous. However, the intensity of PbS/Fe_3O_4 is higher as radiative recombination between electron and hole in Fe_3O_4 shell region

CHAPTER 5

CONCLUSION

5.1 Conclusion

In this study, PbS semiconductor quantum dots (QDs) with near-infrared (NIR) PL were synthesized by using colloidal method. From Brus equation, the estimate size of PbS QDs is 10 nm. We then succesfully synthesis Fe_3O_4 powder with crystallite size of 19 nm. The XRD on the Fe_3O_4 sample confirmed that it is a magnetite nanoparticle. Our sample which is PbS/ Fe_3O_4 at different temperature have been synthesized by using microwave – assisted methods. The further charazteriztion on PbS and PbS/Fe_3O_4 at 45,50,55 ^oC was conducted by Ultraviolet-visible(UV-Vis) and photoluminescence (PL) spectroscopy.

The UV-Vis spectroscopy shows that PbS semiconductor QDs is 1.06 eV for indirect bandgap while 2.23 for direct bandgap. When we coated PbS with Fe3O4 at temperature 45,50 and 55 ^oC, we obtained indirect bandgap energy is 1.00 eV,1.37 eV and 1.25 eV while for direct bandgap are 2.27 eV,2.19 eV and 2.21 eV respectively. As the bandgap energy is from 0-3 eV, we expected that our sample is semiconductor.

Photoluminescence (PL) spectroscopy revealed that emission can reach 1610 nm at near infrared wavelengths. When the temperature of PbS/Fe_3O_4 core shell QDs rises, the wavelength emission redshifts from 475 nm to 506 nm and 539 nm. We assume this emission happens in the

Fe_3O_4 shell since other articles have documented Fe_3O_4 emission at roughly 540 nm and charge carrier delocalization within the shell in inverse type 1 CSQDs. Following that, the wavelength of PbS/Fe_3O_4 core shell QDs rose with temperature due to the thicker shell. The bandgap energy from UV-Vis and PL should have been the same, but we got different results because of Stokes shift.

5.2 Recommendation for future research

There are some future work suggestions that might be suggested for this study. Because of PbS and PbS/Fe_3O_4 core shell quantum dots is precipitated after one weeks, so we suggest that the PbS and PbS/Fe_3O_4 core shell QDs should be characterized as soon as possible. This is because the structure of sample change with time. Finally, the samples can be examined with high resolution transmission electron microscopy (HRTEM) to prove the the formation of Fe_3O_4 shell on PbS core. HRTEM also can be used to examine the exact size of QDs. Other useful suggestion is the complete calculation on Monolayer (ML) of Fe_3O_4 shell on PbS core should be done before entering the lab. As a result, the synthesis process will be more smooth, and we will save a significant amount of time when synthesising the sample.

REFERENCES

Abdi-Jalebi, M., Ibrahim Dar, M., Sadhanala, A., Johansson, E. M. J., & Pazoki, M. (2019). Optical absorption and photoluminescence spectroscopy. In *Characterization Techniques for Perovskite Solar Cell Materials*.

AbouElhamd, A. R., Al-Sallal, K. A., & Hassan, A. (2019). Review of core/shell quantum dots technology integrated into building's glazing. *Energies*.

Aeberhard, U., Vaxenburg, R., Lifshitz, E., & Tomić, S. (2012). Fluorescence of colloidal PbSe/PbS QDs in NIR luminescent solar concentrators. *Physical Chemistry Chemical Physics*.

Ahmadi, S., Chia, C. H., Zakaria, S., Saeedfar, K., & Asim, N. (2012). Synthesis of Fe_3O_4 nanocrystals using hydrothermal approach. *Journal of Magnetism and Magnetic Materials*.

Ajibade, P. A., & Oluwalana, A. E. (2020). Structural, optical, photocatalytic and electrochemical studies of PbS nanoparticles. *Journal of Nano Research*.

Alizadeh-Ghodsi, M., Pourhassan-Moghaddam, M., Zavari-Nematabad, A., Walker, B., Annabi, N., & Akbarzadeh, A. (2019). State-of-the-Art and Trends in Synthesis, Properties, and Application of Quantum Dots-Based Nanomaterials. *Particle and Particle Systems Characterization*.

Allen, P. M., Liu, W., Chauhan, V. P., Lee, J., Ting, A. Y., Fukumura, D., Jain, R. K., & Bawendi, M. G. (2010). InAs(ZnCdS) auantum dots optimized for biological imaging in the near-infrared. *Journal of the American Chemical Society*.

Aswathy, R. G., Yoshida, Y., Maekawa, T., & Kumar, D. S. (2010). Near-infrared quantum dots for deep tissue imaging. *Analytical and Bioanalytical Chemistry*.

Baghbanzadeh, M., Carbone, L., Cozzoli, P. D., & Kappe, C. O. (2011). Microwave-assisted synthesis of colloidal inorganic nanocrystals. *Angewandte Chemie - International Edition*.

Bakueva, L., Gorelikov, I., Musikhin, S., Zhao, X. S., Sargent, E. H., & Kumacheva, E. (2004). PbS quantum dots with stable efficient luminescence in the near-IR spectral range. *Advanced Materials*.

Bederak, D., Balazs, D. M., Sukharevska, N. V., Shulga, A. G., Abdu-Aguye, M., Dirin, D. N., Kovalenko, M. V., & Loi, M. A. (2018). Comparing Halide Ligands in PbS Colloidal

Quantum Dots for Field-Effect Transistors and Solar Cells. *ACS Applied Nano Materials*.

Frecker, T., Bailey, D., Arzeta-Ferrer, X., McBride, J., & Rosenthal, S. J. (2016). Review—Quantum Dots and Their Application in Lighting, Displays, and Biology. *ECS Journal of Solid State Science and Technology*.

Greben, M., Fucikova, A., & Valenta, J. (2015). Photoluminescence quantum yield of PbS nanocrystals in colloidal suspensions. *Journal of Applied Physics*.

Habtemariam, A. B. (2021). Biosynthesis of Magnetite (Fe3O4) Nanostructures using Vernonia Amygdalina Leaves Extract. *Letters in Applied NanoBioScience*.

Hao, J., Liu, H., Miao, J., Lu, R., Zhou, Z., Zhao, B., Xie, B., Cheng, J., Wang, K., & Delville, M. H. (2019). A facile route to synthesize CdSe/ZnS thick-shell quantum dots with precisely controlled green emission properties: towards QDs based LED applications. *Scientific Reports*.

He, Y., Lu, H. T., Sai, L. M., Lai, W. Y., Fan, Q. L., Wang, L. H., & Huang, W. (2006). Microwave-assisted growth and characterization of water-dispersed CdTe/CdS core-shell nanocrystals with high photoluminescence. *Journal of Physical Chemistry B*.

Hines, M. A., & Scholes, G. D. (2003). Colloidal PbS Nanocrystals with Size-Tunable Near-Infrared Emission: Observation of Post-Synthesis Self-Narrowing of the Particle Size Distribution. *Advanced Materials*.

Holder, C. F., & Schaak, R. E. (2019). Tutorial on Powder X-ray Diffraction for Characterizing Nanoscale Materials. *ACS Nano*.

Jin, X., Bai, J., Gu, X., Chang, C., Shen, H., Zhang, Q., Li, F., Chen, Z., & Li, Q. (2017). Efficient light-emitting diodes based on reverse type-I quantum dots. *Optical Materials Express*, *7*(12), 4395.

Kagan, C. R., Lifshitz, E., Sargent, E. H., & Talapin, D. V. (2016). Building devices from colloidal quantum dots. *Science*.

Kargozar, S., Hoseini, S. J., Milan, P. B., Hooshmand, S., Kim, H. W., & Mozafari, M. (2020). Quantum Dots: A Review from Concept to Clinic. *Biotechnology Journal*.

Khalil, M. I. (2015). Co-precipitation in aqueous solution synthesis of magnetite nanoparticles using iron(III) salts as precursors. *Arabian Journal of Chemistry*.

Khoshnam, M., & Salimijazi, H. (2021). Synthesis and characterization of magnetic-photocatalytic Fe3O4/SiO2/a-Fe2O3 nano core-shell. *Surfaces and Interfaces*.

Kortan, A. R., Hull, R., Opila, R. L., Bawendi, M. G., Steigerwald, M. L., Carroll, P. J., & Brus, L. E. (1990). Nucleation and Growth of CdSe on ZnS Quantum Crystallite Seeds, and Vice Versa, in Inverse Micelle Media. *Journal of the American Chemical Society*.

Lagally, M. G. (1985). 5. Diffraction Techniques. *Methods in Experimental Physics*.

Laverdant, J., de Marcillac, W. D., Barthou, C., Chinh, V. D., Schwob, C., Coolen, L., Benalloul, P., Nga, P. T., & Maitre, A. (2011). Experimental Determination of the Fluorescence Quantum Yield of Semiconductor Nanocrystals. *Materials*.

Li, C., Wei, Y., Liivat, A., Zhu, Y., & Zhu, J. (2013). Microwave-solvothermal synthesis of Fe3O4 magnetic nanoparticles. *Materials Letters*.

Li, J. J., Wang, Y. A., Guo, W., Keay, J. C., Mishima, T. D., Johnson, M. B., & Peng, X. (2003). *0028.J.Am.Chem.Soc.2003,125,12567.pdf*.

Mahler, B., Nadal, B., Bouet, C., Patriarche, G., & Dubertret, B. (2012). Core/shell colloidal semiconductor nanoplatelets. *Journal of the American Chemical Society*.

Mahmud, N., Nasser, M. S., El-Naas, M. H., Ba-Abbad, M. M., Wahab Mohammad, A., Mansour, S., & Benamor, A. (2020). Synthesis and Characterization of Fe_3O_4 Nanoparticles Using Different Experimental Methods. *IOP Conference Series: Materials Science and Engineering*.

Mäntele, W., & Deniz, E. (2017). UV–VIS absorption spectroscopy: Lambert-Beer reloaded. *Spectrochimica Acta - Part A: Molecular and Biomolecular Spectroscopy*.

Marand, Z. R., Helmi, M., Farimani, R., & Shahtahmasebi, N. (2014). Study of magnetic and structural and optical properties of Zn doped Fe 3 O 4 nanoparticles synthesized by co-precipitation method for biomedical application Properties of Zn doped Fe 3 O 4 nanoparticles. *Nanomed J*.

Matsuoka, M., Saito, M., & Anpo, M. (2012). Photoluminescence Spectroscopy. *Characterization of Solid Materials and Heterogeneous Catalysts: From Structure to Surface Reactivity, Volume 1&2*.

Mekis, I., Talapin, D. V., Kornowski, A., Haase, M., & Weller, H. (2003). One-pot synthesis of highly luminescent CdSe/CdS core-shell nanocrystals via organometallic and “greener” chemical approaches. *Journal of Physical Chemistry B*.

Moreels, I., Lambert, K., Smeets, D., & De Muynck, D. (2009). Size-Dependent Optical Properties of Colloidal PbS Quantum Dots - ACS Nano (ACS Publications). *Acs Nano*.

Nanda, K. K., Kruis, F. E., Fissan, H., & Behera, S. N. (2004). Effective mass approximation for two extreme semiconductors: Band gap of PbS and CuBr nanoparticles. *Journal of Applied Physics*.

Pan, Z., Zhang, H., Cheng, K., Hou, Y., Hua, J., & Zhong, X. (2012). *Highly E ffi cient Inverted Type-I CdS / CdSe Core / Shell Structure*.

Peng, X., Schlamp, M. C., Kadavanich, A. V., & Alivisatos, A. P. (1997). Epitaxial growth of highly luminescent CdSe/CdS core/shell nanocrystals with photostability and electronic accessibility. *Journal of the American Chemical Society*.

Penner, M. H. (2017). *Basic Principles of Spectroscopy*.

Pichaandi, J., & Van Veggel, F. C. J. M. (2014). Near-infrared emitting quantum dots: Recent progress on their synthesis and characterization. *Coordination Chemistry Reviews*.

Purcar, V., Rădiţoiu, V., Nichita, C., Bălan, A., Rădiţoiu, A., Căprărescu, S., Raduly, F. M., Manea, R., Şomoghi, R., Nicolae, C. A., Raut, I., & Jecu, L. (2021). Preparation and characterization of silica nanoparticles and of silica-gentamicin nanostructured solution obtained by microwave-assisted synthesis. *Materials*.

Reiss, P., Protière, M., & Li, L. (2009). Core/shell semiconductor nanocrystals. *Small*.

Ren, F., Zhao, H., Vetrone, F., & Ma, D. (2013). Microwave-assisted cation exchange toward synthesis of near-infrared emitting PbS/CdS core/shell quantum dots with significantly improved quantum yields through a uniform growth path. *Nanoscale*.

Resch-Genger, U., & Rurack, K. (2013). Determination of the photoluminescence quantum yield of dilute dye solutions (IUPAC Technical Report). *Pure and Applied Chemistry*.

Rodríguez-Mas, F., Ferrer, J. C., Alonso, J. L., Valiente, D., & de Ávila, S. F. (2020). A comparative study of theoretical methods to estimate semiconductor nanoparticles' size. *Crystals*.

Sadat, M. E., Kaveh Baghbador, M., Dunn, A. W., Wagner, H. P., Ewing, R. C., Zhang, J., Xu, H., Pauletti, G. M., Mast, D. B., & Shi, D. (2014). Photoluminescence and photothermal effect of Fe3O4nanoparticles for medical imaging and therapy. *Applied Physics Letters*.

Sagala, L. P. S., Humaidi, S., Tarigan, K., Soehada, A. M. S., & Sebayang, P. (2021). Synthesis and characterization of nanoparticles Zn0.7Ni0.15Cu0.15Fe2O4 using the co-precipitation method. *Journal of Physics: Conference Series*.

Sai, L. M., & Kong, X. Y. (2011). Microwave-assisted synthesis of water-dispersed CdTe/CdSe

core/shell type II quantum dots. *Nanoscale Research Letters*.

Singh, M., Goyal, M., & Devlal, K. (2018). Size and shape effects on the band gap of semiconductor compound nanomaterials. *Journal of Taibah University for Science*.

Smith, A. M., & Nie, S. (2010). Semiconductor nanocrystals: Structure, properties, and band gap engineering. *Accounts of Chemical Research*.

Sohn, P. R. (2018). *Synthesis of Lead Sulfide Quantum Dots and their Ligands for Photon Upconversion Applications By Philip Robin Sohn A thesis submitted in conformity with the requirements for the degree of Master of Science Department of Chemistry University of Toronto © C*.

Strehlow, W., & Cook, E. (1973). Energy Band Gaps in Semiconductors and Insulators. *Journal of Physical Chemistry, Ref. Data*.

Stride, J. A., & Mirnajafizadeh, F. (2020). A Brief Review on Core/shell Quantum Dots. *SDRP Journal of Nanotechnology & Material Science*.

Subramanian, S., Ganapathy, S., Rajaram, M., Subramanian, S., Ayyaswamy, A., & Ramasamy, J. (2020). Effect of core size on the luminescence properties of cadmium telluride/zinc sulphide core-shell quantum dots. *Materials Today: Proceedings*.

Touati, B., Gassoumi, A., Alfaify, S., & Kamoun-Turki, N. (2015). Optical, morphological and electrical studies of Zn:PbS thin films. *Materials Science in Semiconductor Processing*.

Tzafaras, N., Adlhart, W., & Jagodzinski, H. (1981). High-temperature investigations of magnetite (Fe 3 O 4) . *Acta Crystallographica Section A Foundations of Crystallography*.

Vale, B. R. C., Silva, F. O., Carvalho, M. S., Raphael, E., Ferrari, J. L., & Schiavon, M. A. (2016). Water-soluble cdte/cds core/shell semiconductor nanocrystals: How their optical properties depend on the synthesis methods. *Crystals*.

Vallikkodi, M. (2018). *Synthesis, Growth and Characterization of Piperazinium p-Aminobenzoate and Piperazinium p-Chlorobenzoate Nonlinear Optical Single Crystals*.

Vasudevan, D., Gaddam, R. R., Trinchi, A., & Cole, I. (2015). Core-shell quantum dots: Properties and applications. *Journal of Alloys and Compounds*, *636*(February).

Wieliczka, B. M., Kaledin, A. L., Buhro, W. E., & Loomis, R. A. (2018). Wave Function Engineering in CdSe/PbS Core/Shell Quantum Dots. *ACS Nano*.

Yan, A., Liu, X., Qiu, G., Wu, H., Yi, R., Zhang, N., & Xu, J. (2008). Solvothermal synthesis and

characterization of size-controlled Fe3O4 nanoparticles. *Journal of Alloys and Compounds*.

Yang, X., Ren, F., Wang, Y., Ding, T., Sun, H., Ma, D., & Sun, X. W. (2017). Iodide capped PbS/CdS core-shell quantum dots for efficient long-wavelength near-infrared light-emitting diodes. *Scientific Reports*.

Zaini, M. S., Kamarudin, M. A., Ying Chyi, J. L., Alang Ahmad, S. A., & Mohmad, A. R. (2019). Temperature and power dependence of photoluminescence in PbS quantum dots nanoparticles. *Sains Malaysiana*.

Zaini, M. S., Ying, J., Liew, C., Ainliah, S., Ahmad, A., Mohmad, A. R., & Kamarudin, M. A. (2020). applied sciences Quantum Confinement E ff ect and Photoenhancement of Photoluminescence of PbS and PbS / MnS Quantum Dots. *Applied Sciences*.

Zhang, M., Yue, J., Cui, R., Ma, Z., Wan, H., Wang, F., Zhu, S., Zhou, Y., Kuang, Y., Zhong, Y., Pang, D. W., & Dai, H. (2018). Bright quantum dots emitting at ~1,600 nm in the NIR-IIb window for deep tissue fluorescence imaging. *Proceedings of the National Academy of Sciences of the United States of America*.

Zhao, X., Gorelikov, I., Musikhin, S., Cauchi, S., Sukhovatkin, V., Sargent, E. H., & Kumacheva, E. (2005). Synthesis and optical properties of thiol-stabilized PbS nanocrystals. *Langmuir*.

Zhong, X., Xie, R., Zhang, Y., Basché, T., & Knoll, W. (2005). High-quality violet- To red-emitting ZnSe/CdSe core/shell nanocrystals. *Chemistry of Materials*.

APPENDICES

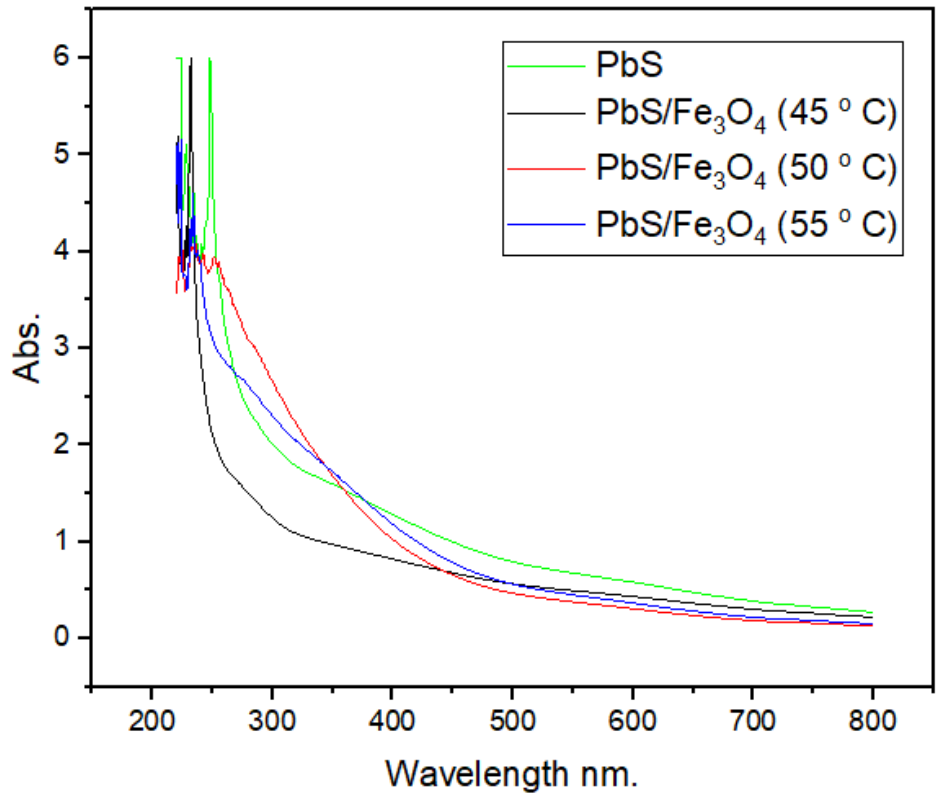

The graph show UV-vis absorption of PbS and PbS/Fe_3O_4 at different temperature against wavelength

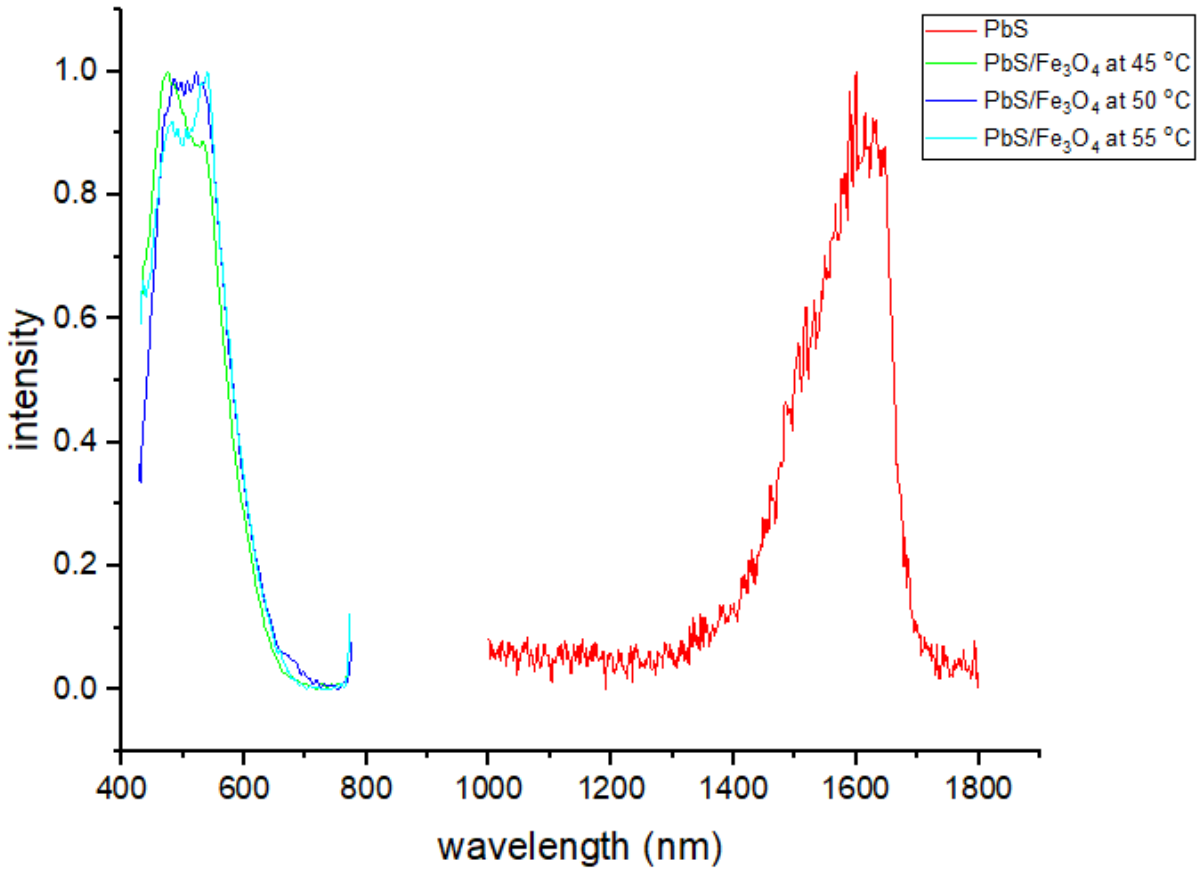

The graph shows the Normalized Photoluminescence of PbS and PbS/Fe_3O_4 at different temperature

CALCULATION OF ESTIMATED MONOLAYER (ML) OF SHELL

Volume of PbS core = $\frac{4}{3}\pi\ (4\ nm\ )^3 = 268.08\ nm^3$

Volume of one unit cubic PbS = $(0.594\ nm)^3 = 0.209\ nm^3$

1 unit of cubic = 0.209 nm^3

If $268.08\ nm^3$, so unit of cubic = $\frac{268.08\ nm^3}{0.209\ nm^3}$ = 1283 unit of PbS

PbS is Face center cubic (has 4 atom) , so in one unit cell (4 Pb + 4 S)

Atom = 1283 unit of PbS x 8 atom = 10264 atom of PbS in 1 QDs

∴ **1 QDs have 10264 atom of PbS**

In 5 ml PbS (5 ml Pb + 0.245 ml S)

Pb,

Number of Mol = $\frac{MV}{1000}$ = $\frac{0.0166x\ 5\ ml}{1000}$ = 0.000083 mol

Atom = mol x Avogadro constant =0.000083 mol x ($6.02 \times\ 10^{23}\ \ mol^{-1}$) =4.9966 x 10^{19}

S,

Number of Mol = $\frac{MV}{1000}$ = $\frac{0.1x\ 0.245\ ml}{1000}$ = 2.45 x 10^{-5} mol

Atom = mol x Avogadro constant =2.45 x 10^{-5} mol x ($6.02 \times\ 10^{23}\ \ mol^{-1}$) = 1.47 x 10^{19}

Total PbS in 5 ml ,

Pb +S =4.9966 x 10^{19} + 1.47 x 10^{19} = 6.47 x 10^{19}

S x 2= 1.47 x 10^{19} x 2 = 2.94 x 10^{19} (assume all S is used)

∴ Pb has 2.94 x 10^{19} atom in 5 ml solution

We know 1 QDs have 10264 atom of PbS

If 2.94 x 10^{19} atom of Pb , we have $\frac{1}{10264\ atom}$ x 2.94 x 10^{19} atom = 2.86 x 10^{15} PbS QDs

Mol of Fe_3O_4 = $\frac{\text{molarity} \times \text{volume}}{1000}$ = $\frac{0.1\ \text{M} \times 0.1\ \text{ml}}{1000}$ = 0.00001 mol

Atom = mol x Avogadro constant = 0.00001 mol x (6.02 × 10^{23} mol^{-1}) = 6.02 × 10^{18} atom

∴ 0.1 ml Fe_3O_4 have 6.02 × 10^{18} atom

1 monolayer = 0.84 nm

If 1 ML,

Volume of shell+ core = $\frac{4}{3}\pi\ (4\ \text{nm} + 0.84\ \text{nm})^3 = 475\ \text{nm}^3$

Volume of shell = (Volume of shell+ core)- (Volume of PbS core)

= 475 nm^3 -268.08 nm^3

= 207 nm^3

1 unit of cubic = 0.84 nm^3

If 207 nm^3 , so unit cell of Fe_3O_4 is $\frac{207\ nm^3}{0.84\ nm^3}$ = 246 unit

Fe_3O_4 is face center cubic with 8 lattice point,

=246(8) = 1968 atom

Atom need to grow shell,

=2.86 x 10^{15} PbS QDs x (1968 atom of Fe_3O_4)

=5.64 x 10^{18} atom of Fe_3O_4 needed for 1ML

5.64 x 10^{18} atom Fe_3O_4 = 1 ML

If 6.02 × 10^{18} atom, we get $\frac{1}{5.64\ x\ 10^{18}}$x 6.02 × 10^{18} = 1.07 ML

∴ 1.07 ML or 0.90 nm is the thickness of shell